Characterisation of the impact induced damage in composites by cross-comparison among experimental non-destructive evaluation techniques and numerical simulations

Original Article

Institution of MECHANICAL ENGINEERS
Journal of MECHANICAL ENGINEERING SCIENCE

Proc IMechE Part C:
J Mechanical Engineering Science
2017, Vol. 231(16) 3077–3090

DOI: 10.1177/0954406216681595
journals.sagepub.com/home/pic
SAGE

Characterisation of the impact induced damage in composites by cross-comparison among experimental non-destructive evaluation techniques and numerical simulations

A Riccio, S Saputo, A Sellitto and V Lopresto

Abstract

Composite fibre-reinforced materials, under low velocity impacts, can experience simultaneous interacting failure phenomena, such as intra-laminar damage, fibre breakage and matrix cracking, and inter-laminar damage such as delaminations. These failure mechanisms are usually the subject of extensive investigations because they can cause a significant reduction in strength of composites structures leading to premature failure. In the present work, composite plates under low velocity impact are investigated. Experimental data, such as experimental curves and images from non-destructive inspections, are used to characterise the low velocity impacts-induced damage in conjunction with a non-linear explicit Finite element numerical model. The adopted numerical model, implemented in the FE code (Abaqus/Explicit) by a user-defined material subroutine (VUMAT), has been demonstrated to be very effective in predicting the damage onset and evolution and, in general, able to correctly integrate the experimental data by providing useful information about the impact damage localisation and evolution.

Keywords

Thermal imaging, ultrasound, impact mechanics, FEA, structural mechanics

Date received: 27 May 2016; accepted: 4 November 2016

Introduction

Composite materials are widely used for railways, aerospace, naval and automotive applications due to their excellent properties in terms of specific strength and stiffness. However, when subjected to low velocity impacts, these materials show a limited damage tolerance. Indeed, the damages induced by low velocity impacts, such as in plane damage (fibre breakage and matrix cracking) and out of plane damage (delaminations), are not easily detectable by visual inspections and, usually, lead to a considerable reduction of carrying load capability. The damage phenomena induced by low velocity impacts have been investigated in literature, both from a numerical and an experimental point of view.

Generally, expensive experimental campaigns are necessary to determine material property and to better appreciate the failure mechanisms.[1–8] Indeed, as demonstrated by experimental tests, specimen impact response can be influenced by different parameters such as microstructure and hygro-thermal conditions.[9] In literarure[10,11] the influence of the punch size on the response of the composite specimen in terms of stiffness, peak force, deflection, and energy dissipations is experimentally investigated. Non-destructive techniques are adopted to monitor the damage status after impact in literarure.[12–17] Infrared thermography and selectively heating thermography (SeHT) have been widely used to detect the different damages in impacted composites plates, thanks to thermal maps,[12–14] while ultrasound techniques have been used, respectively, to detect the damage in impacted composite structures in Grimberg et al.[16] and to

Department of Industrial and Information Engineering, Second University of Naples, Aversa, Italy

Corresponding author:
A Riccio, Department of Industrial and Information Engineering, Second University of Naples, via Roma 29, Aversa 81031, Italy.
Email: aniello.riccio@unina2.it

evaluate the interfaces and inter-laminar mechanical properties of composite plates in Gros.[17]

Indeed, in order to reduce the experimental campaigns costs associated to the understanding and prediction of damage induced in composite materials by low velocity impacts, it is compulsory to develop a model that reproduces as faithfully as possible the structure deformation and the energy dissipation.

Several studies about impact phenomena, in literature, introduce failure predictive models and the associated underlying critical aspects related to the impact events.[4–9,18–20] An interesting overview on numerical models for the prediction of onset and growth of intra-laminar damage is given in literature[20–30] where limitations of the stress-based continuum damage models, adopted for the fibre breakage and matrix cracking prediction, in the presence of localised failure phenomena, involving localised stress and material discontinuities, are pointed out. This is the reason why intra-laminar damage onset and growth is usually predicted by means of CDM (Continuum Damage Models), introducing a degradation factor to take into account the mechanical material properties variations.[31] CDM has been then implemented in FE codes to model the progressive intra-laminar degradation of advanced composite materials. In Puck and Schurmann,[32] a 2D CDM-based model for woven composite laminates under impact loading has been developed and implemented. Later on in Donadon[33] this model has been further extended by including 3D effects. In literature,[34,35] a 3D failure model for laminates, based on the Puck's theory, has been developed.

Numerical models for the simulation of inter-laminar damage on-set and evolution, based on Virtual Crack Closure Technique (VCCT) and Cohesive Zone Model (CZM), are presented in literature.[21,27,36–38] The limitations of VCCT, with respect to CZM, related to the need of a pre-existing crack and to the use of adaptive re-meshing tools, are pointed out. In literature,[25–27] the delaminations' onset due to low velocity impacts is simulated by using cohesive elements between adjacent plies. However, it has been demonstrated[39–42] that the numerical results are mesh size dependent. This issue has been mitigated by introducing energy-based criteria[43–48] and considering the fracture energy distributed over the volume of the elements.

A number of works[49–55] investigate both numerical and experimental aspects of complex composite structures under low velocity impacts condition.

In Riccio et al.,[50,51] CZM and CDM, respectively, for inter-laminar and intra-laminar failure predictions, are adopted to numerically study the evolution of damage mechanisms in composite panels under low velocity impacts. In Riccio et al.,[51] the study has been performed in combination with NDT results.

In order to fully understand the impact damage mechanisms formation and evolution, a concurrence of different experimental techniques is recommended able to adequately represent the global behaviour of the impacted structure and the damage evolution in the localised impact area. In the present paper, the numerical model presented in Riccio et al.[51] has been enhanced by introducing alternative intra-laminar failure criteria which can be used in conjunction with brick finite elements providing a true three-dimensional stress distribution. The numerically predicted material response has been correlated with experimental data provided by CNR (Italian National Council of Research) and already published in Riccio et al.,[51] in terms of NDT results and force vs. time, energy vs. time, and force vs. displacements on composite plates impacted according to three different impact energy values. The aim of this paper was to use experimental data from different sources (NDT results from ultrasounds and thermography and force vs. time, energy vs. time, and force vs. displacements curves obtained during the impact test) in conjunction with an enhanced non-linear explicit finite element numerical model to investigate and understand the impact behaviour of composite plates. The formation and the evolution of impact induced intra-laminar and inter-laminar damages have been taken into account. At this aim, the experimental data in terms of force and energy vs. time and displacements curves allowed to fully analyse the global mechanical impact behaviour of the investigated plates while NDT results gave useful information on the impact induced damage evolution.

In the Experimental activities section, a brief description of the experimental procedures adopted during the impact and the non-destructive tests, fully described in Riccio et al.,[51] is reported. In the Numerical models section, detailed information on the numerical model, implemented in the FEM code ABAQUS explicit by means of a user subroutine, is provided. Finally, in the Experimental and numerical results section, the numerical results are given and compared with the experimental data. The correlation between numerical and experimental data is, then, discussed and critically assessed.

Experimental activities

In this section, the experimental setup of the impact and non-destructive tests, performed on the investigated composite plates, are briefly introduced for the sake of completeness and clarity of the present paper. The complete description of these experimental activities can be found in Riccio et al.[51]

Experimental setup of the impact test

The 'prEN 6038' standard from the European association of Aerospace Manufacturers (AECMA) has been adopted for the manufacturing and for the impact test on the investigated composite panels.

A drop tower system has been adopted for the drop test reproducing low velocity impact conditions. Three different impact tests have been performed, assuming different energy values by changing the height h and, consequently, the velocity v_0 of the impactor.

The investigated composite panels are rectangular plates (150 mm × 100 mm), placed on a fixture with a rectangular cut-out (125 mm × 75 mm). A hemispherical impactor with 8 mm radius and 3.64 kg mass has been adopted to impact the panels. The material adopted is a carbon-epoxy unidirectional pre-preg (a variant of the G1157/RTM-6 material system) fully characterised in the frame of a confidential scientific Italian research project. Each ply has a thickness of 0.3 mm, and the stacking sequence of the specimens is $[0/90/45/–45]_s$.

Non-destructive tests

Non-destructive tests have been carried out on the impacted specimens, using infrared lock-in thermography and ultrasound.

In the frame of the thermography tests, the panels have been heated up by a modulated light and the resulting surface temperature variations have been acquired by a thermal camera. The thermal energy provided to the specimens is partially reflected by the specimen, producing an interference with the incoming modulated light whose pattern can be measured. The amplitude of this pattern is a measure of the amount of thermal energy transferred to the plate, while the phase can be associated to the reflected thermal waves. The theoretical aspects of this method are more in-depth analysed in Riccio et al.[51]

For the Ultrasonic tests, the Pulse Echo technique has been adopted. This technique is based on the propagation of ultrasonic waves into the specimen in order to identify the damage area. The ultrasonic waves are transmitted by an emitting probe, which is able to capture the echo signal.

The C-scan and A-scan envelops have been used to collect and display the ultrasonic data. The C-scan provides a 2D representation of the size and location of the damaged area. In this work, the C-Scans have been obtained by adopting the Olympus OmniScan® SX Phased array automated data acquisition system with a 16:64PR phased array unit.

The A-scan envelope provides a representation of the incoming ultrasound echo energy as a function of the time. The data are acquired by the Staveley Instruments BondMasterTM 1000 composite tester in resonance mode according to Riccio et al.[51] In this work, the A-scan rough data were not reported. To get an alternative representation of the damaged area, an envelope of failure points obtained from the A-scan has been plotted with a 1 mm × 1 mm resolution grid.

Numerical models

Numerical models for inter-laminar damage

To study onset and propagation of inter-laminar damage in the investigated composite plates, cohesive zone model (CZM)-based elements have been adopted. Cohesive elements are able to predict strength, stiffness and fracture toughness for each different layer interface. Cohesive constitutive response is characterised by two different phases, an initial damage phase and an evolution damage phase, with removal of the elements when fully damaged (Figure 1).

Abaqus FEM code allows to define two different failure initiation criteria, delimiting the initial damage phase of the traction-separation law, namely the maximum nominal stress criterion (MAXS) and the quadratic nominal stress criterion (QUADS). Both criteria are stress based, but the MAXS criterion does not assume any relation between different stress directions. On the other hand, QUADS criterion considers the contribution of nominal stress and

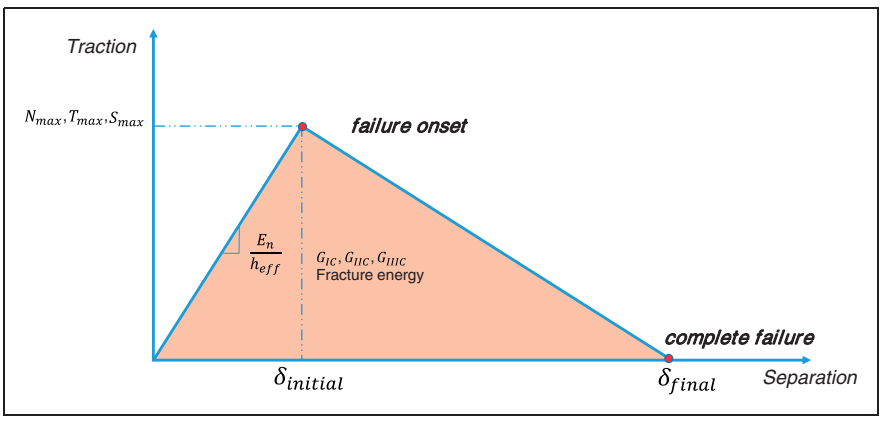

Figure 1. Traction-separation law for cohesive elements.

allowable stress for all different directions in a quadratic form.

Maximum nominal stress criterion (*MAXS*)

$$MAX\left\{\frac{\sigma_n}{N_{MAX}}, \frac{\sigma_t}{T_{MAX}}, \frac{\sigma_s}{S_{MAX}}, \right\} = 1$$

Quadratic nominal stress Criterion (*QUADS*)

$$\left(\frac{\sigma_n}{N_{MAX}}\right)^2 + \left(\frac{\sigma_t}{T_{MAX}}\right)^2 + \left(\frac{\sigma_s}{S_{MAX}}\right)^2 = 1$$

- N_{max} is the nominal stress in the pure normal mode;
- T_{max} is the nominal stress in the first shear direction and
- S_{max} is the nominal stress in the second shear direction.

Abaqus FEM code allows to define different failure evolution criteria for cohesive element, the 'Power law (PW)', the 'Benzeggagh-Kenane (BK)' and a degradation criteria implemented by the user in a tabular form. In Table 1, the PW and the BK failure evolution criteria are reported.

In this table, G_j is the energy release rate associated to the fracture mode j and G_{jc} is the critical energy release rate associated to the fracture mode j. (According to the adopted notations, G_{Ic} is the normal mode fracture energy, G_{IIc} is the shear mode fracture energy first direction, and G_{IIIc} is the shear mode fracture energy second direction). α and η are empirical coefficients (generally ranging between 1 and 1.6) obtained from experimental campaigns. For isotropic fractures, $G_{Ic} = G_{IIc}$ and the material response is independent from η coefficient. Finally, $G_{SHEAR} = G_{II} + G_{III}$; $G_T = G_I + G_{SHEAR}$.

The QUADS criterion in combination with the PW criterion has been used throughout the present paper.

Table 1. Failure evolution criteria.

Power law (PW)	$\left(\frac{G_I}{G_{Ic}}\right)^{\alpha} + \left(\frac{G_{II}}{G_{IIc}}\right)^{\alpha} + \left(\frac{G_{III}}{G_{IIIc}}\right)^{\alpha} = 1$
Benzeggagh-Kenane (BK)	$G_{Ic} + (G_{IIc} - G_{Ic})\left(\frac{G_{SHEAR}}{G_T}\right)^{\eta} = G_{Tc}$

Numerical models for intra-laminar damage (USER DEFINED MATERIAL in ABAQUS)

The intra-laminar damage model introduced in the present paper is based on a continuum damage mechanics approach, where the internal state variables are damage variables (d_i) that reduce the material stiffness degradation in order to simulate the progressive intra-laminar damage evolution. In ABAQUS, generally, Hashin failure criteria formulation[48–53] is adopted for the intra-laminar failure mode prediction. Hashin failure criteria allow to take into account the different failure modes such as fibre tensile and compression failure, and matrix tensile and compression cracking. By the way, alternative criteria can be defined and implemented in Abaqus/Explicit by means of user-defined material subroutine. The proposed intra-laminar damage model adopts user-defined criteria, implemented in ABAQUS explicit by means of a user-defined material subroutine, which are summarised in Table 2.

In Table 2, $\hat{\sigma}_{ij}$ are components of the effective stress tensor evaluated at integration points during the iterations. This progressive damage method offers a general capability of modelling progressive intra-laminar damage in fibre-reinforced composites. The constitutive relation adopted for each failure mode can be graphically represented by the trend shown in Figure 2.

Also for the intra-laminar damage, two different phases can be identified, the damage initiation phase and the propagation phase. The point A in Figure 2 identifies the limit stress value according to the failure initiation criteria, and starting from this point, the increase in stresses causes the degradation of the material properties.

Table 2. User-defined failure criteria.

Hashin Fibre tension $\widehat{\sigma}_{11} > 0$	$F_{ft} = \left(\frac{\widehat{\sigma}_{11}}{X_T}\right)^2 + \left(\frac{\widehat{\sigma}_{12}}{S_L}\right)^2 = 1$
Hashin Fibre Compression $\widehat{\sigma}_{11} < 0$	$F_{fc} = \left(\frac{\widehat{\sigma}_{11}}{X_C}\right)^2 = 1$
Hashin Matrix tension $\widehat{\sigma}_{22} \geqslant 0$	$F_{mt} = \left(\frac{\widehat{\sigma}_{22}}{Y_T}\right)^2 + \left(\frac{\widehat{\sigma}_{12}}{S_L}\right)^2 = 1$
Puck Matrix compression $\widehat{\sigma}_{22} \leqslant 0$	$F_2^{Compr} = \left(\frac{\tau_{nt}}{S_{23}^A - \mu_{nt}\sigma_{nn}}\right)^2 + \left(\frac{\tau_{nl}}{S_{12} - \mu_{nl}\sigma_{nn}}\right)^2 \geqslant 1$
Non linear shear criterion	$F_{i,j} = \frac{\hat{\sigma}_{i,j}}{S_{i,j}} \quad i \neq j$

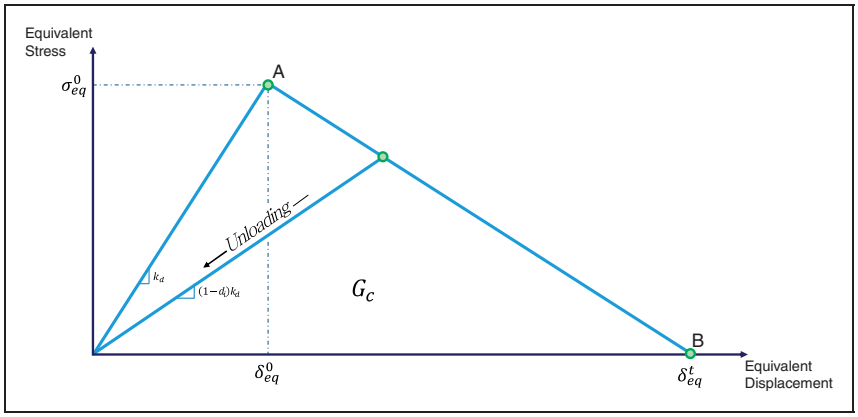

Figure 2. General constitutive relation adopted for each failure mode.

Table 3. Equivalent displacement and stress definition.

Failure mode	δ_{eq}	σ_{eq}
Fibre tension ($\hat{\sigma}_{11} \geqslant 0$)	$L_c\sqrt{\langle\varepsilon_{11}\rangle^2+\alpha\varepsilon_{12}^2}$	$\frac{L_c(\langle\sigma_{11}\rangle\langle-\varepsilon_{11}\rangle+\alpha\sigma_{12}\varepsilon_{12})}{\delta^{ft}_{eq}}$
Fibre compression ($\hat{\sigma}_{11} < 0$)	$L_c\langle-\varepsilon_{11}\rangle$	$\frac{L_c\langle-\sigma_{11}\rangle\langle-\varepsilon_{11}\rangle}{\delta^{fc}_{eq}}$
Matrix tension ($\hat{\sigma}_{22} \geqslant 0$)	$L_c\sqrt{\langle\varepsilon_{22}\rangle^2+\varepsilon_{12}^2}$	$\frac{L_c(\langle\sigma_{22}\rangle\langle\varepsilon_{22}\rangle+\sigma_{12}\varepsilon_{12})}{\delta^{mt}_{eq}}$
Matrix compression ($\hat{\sigma}_{22} < 0$)	$\frac{\sqrt{(\varepsilon_{ln}\cdot L_C)^2+(\varepsilon_{tn}\cdot L_C)^2}}{\sqrt{F_2^{Compr}}}$	$L_c\sqrt{\sigma_{LN}^2+\sigma_{TN}^2}$
Non-linear shear	$L_c\langle-\varepsilon_{i,j}\rangle$ i ≠ j	$\tau_{ij}=c_1\gamma_{ij}+c_2\gamma_{ij}^2+c_3\gamma_{ij}^3$

The degradation has been simulated thanks to the degradation coefficients d_i for the different failure modes. These coefficients are defined by the following relation

$$d_I=\frac{\delta^f_{I,eq}\left(\delta_{I,eq}-\delta^0_{I,eq}\right)}{\delta_{I,eq}\left(\delta^f_{I,eq}-\delta^0_{I,eq}\right)};\ \left(\delta^f_{I,eq}\leqslant\delta_{I,eq}\leqslant\delta^f_{I,eq}\right);\quad I\equiv\{f_c,f_t,m_c,m_t\} \tag{1}$$

where $\delta^0_{I,eq}$ is the equivalent displacement at which the initiation criterion is satisfied, and $\delta_{I,eq}$ is the equivalent displacement at which the material is completely damaged ($d_i=1$). In equation (1), $\delta^f_{I,eq}$ is obtained from the following relation, assuming that the fracture energy G_c is specified and the softening law is linear

$$\delta^f_{I,eq}=\frac{2G_{Ic}}{\sigma^0_{I,eq}} \tag{2}$$

In Table 3, the equivalent stresses and displacements are reported for the four considered failure modes. The degradation damage coefficient d_i ranges between 0 (undamaged state) and 1 (fully damage state) for each failure mode. The damage evolution law is based on the fracture energy dissipated during the damage process, G_c. This evolution law is a generalisation of the approach proposed in Davila et al.[56] for modelling inter-laminar delaminations by cohesive elements.

In Table 3, L_c is the characteristic length of the element, introduced to alleviate mesh dependency during the material softening phase, and ‹› is Macauley bracket operator, defined for every $\gamma \in R$ as

$$\langle\gamma\rangle=\frac{(\gamma+|\gamma|)}{2} \tag{3}$$

Several methods have been proposed for computing the characteristic length. In Bazant and Oh,[57] the following relation for square elements is suggested

$$L_c=\frac{\sqrt{A_{ip}}}{\cos\theta} \tag{4}$$

where A_{ip} is the area related to the integration point and θ is the angle between the crack direction and the element edge.

In general, the introduction of the characteristic length has been found to be very computationally effective for almost-square elements; however, it

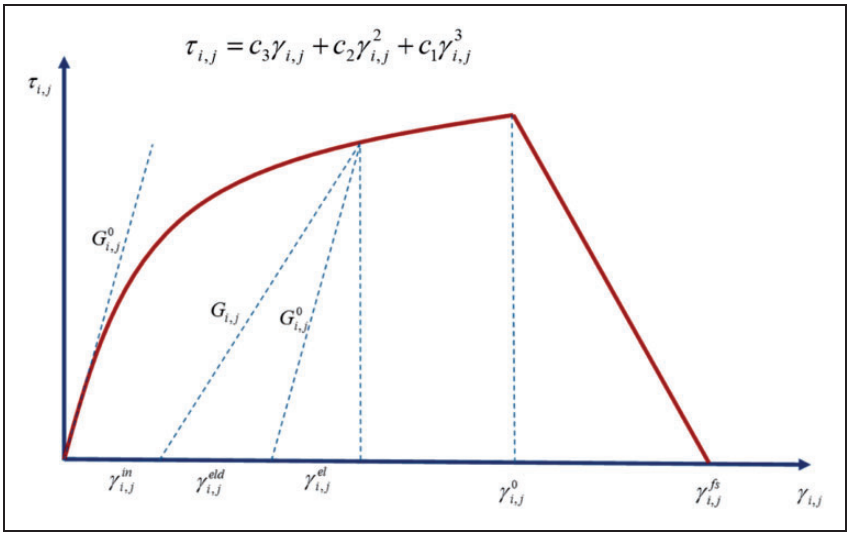

Figure 3. Shear stress–strain response.

does not completely eliminate the mesh dependency issue.

The non-linear shear constitutive relation is illustrated in Figure 3. The experimentally observed non-linear shear trend, for the adopted material system, can be represented by a cubic polynomial stress–strain curve where c_1, c_2, c_3 coefficients are evaluated by fitting the polynomial curve to the experimental obtained shear stress–strain data.[58]

As already pointed out, the adopted failure criteria have been implemented in ABAQUS/Explicit[59] by means of a user-defined material subroutine (VUMAT). In Figure 4, a flow chart schematically representing how the implemented subroutine works is introduced.

At the beginning of the increment, the subroutine evaluates the field variables, starting from the nodal values. In a second step, stress and strain variations are computed. Then the strain and stress values are updated and failure criteria are checked. If the failure criteria are satisfied, the subroutine evaluates the damage variable and updates the stress values.

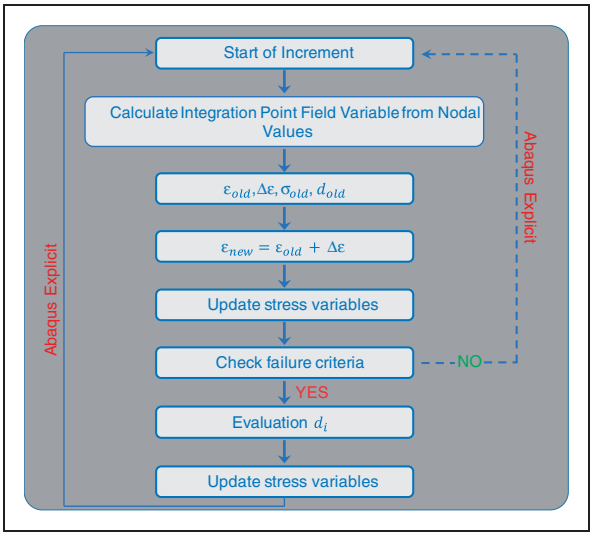

Figure 4. VUMAT flow diagram subroutine for intra-laminar damage model.

Numerical FEM implementation

The geometrical description and the boundary conditions of the tested specimens are shown in Figure 5, while the properties of the adopted material system are introduced in Table 4.

With reference to Figure 5, when assembling the FEM model, the composite plate has been partitioned in two domains: a 'local' domain, which can be identified with the area close to the impact point (60 mm × 60 mm wide), and a 'global' domain covering the rest of the plate. In the local domain, finite elements characterised by 1 mm length and 1 mm width have been adopted, while in the global domain finite elements characterised by 3 mm length and 1 mm width has been introduced. Concerning the distribution of elements along the thickness of the plate, for the 'local' domain, one element-per-ply (0.3 mm thick) has been used, while for the 'global' domain, the whole plate thickness has been covered with only one finite element (2.47 mm thick).

The global domain has been modeled with continuum shell elements (SC8R) while two different FEM models with different element formulations have been introduced for the local domain. According to the first FEM model, the continuum shell elements SC8R have been adopted also in the local domain for the evaluation of intra-laminar damage initiation and evolution, respectively, with the Hashin failure criteria and damage evolution law available in the standard version of the FEM code ABAQUS (see Figure 2 and equation (1)). It should be emphasised that the choice of using continuum shell elements for the local domain in the first FEM

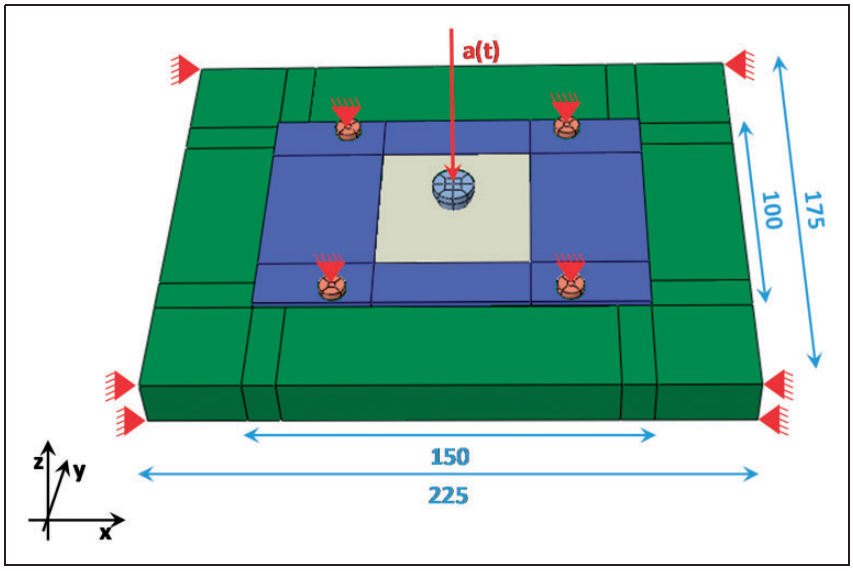

Figure 5. Geometrical description and boundary conditions of the numerical model (length in mm).

Table 4. Material properties.

Properties	Value
Density	1400 kg/m^3
Orthotropic properties	$E_{11} = 130050$ MPa; $E_{22} = E_{33} = 11550$ MPa; $G_{12} = G_{13} = G_{23} = 6000$ Mpa; $\nu_{12} = \nu_{13} = \nu_{23} = 0.312$
Strength	$X_T = 1460.70$ MPa; $X_C = 876.42$ MPa; $Y_T = 77.11$ MPa; $Y_C = 241.43$ MPa; $S_{12} = S_{13} = 90$ MPa; $S_{23} = 40$ MPa
In-plane fracture energies	$GF_{ftC} = 16.40$ kJ/m^2; $GF_{fxC} = 5.90$ kJ/m^2; $GF_{mtC} = 0.5$ kJ/m^2; $GF_{mcC} = 4.62$ kJ/m^2
Inter-laminar fracture toughness	$G_{Ic} = 0.18$ kJ/m^2; $G_{IIc} = 0.5$ kJ/m^2; $G_{IIIc} = 0.5$ kJ/m^2

model is due to the unfeasibility to evaluate intra-laminar damage initiation and evolution with solid elements in the standard ABAQUS version. According to the second FEM model, adopted for the evaluation of intra-laminar damage with the user-defined failure criteria (VMAT), the 'local' domain has been modeled with solid C3D8R finite elements. One layer of Cohesive elements COH3D8, characterised by 0.3 mm length, 0.3 mm width and 0.01 mm thickness, has been introduced at each ply interface in the 'local' domain. The interface properties of the cohesive elements, in particular damage initiation properties related to the Energy Release Rate (ERR), have been evaluated taking into account the scaling effects with respect to the cohesive elements size according to literature[60,61] to avoid inconsistencies in inter-laminar damage propagation prediction. According to Fanteria et al.,[54] the interaction between the cohesive failure mode II and the transverse shear failure has been taken into account by adopting the matrix shear properties for the evaluation of the cohesive parameters related to the mode II of failure.[37,49] The fixture base and the four rigid clamps (with 5 mm radius and 3 mm height), connecting the global plate to the fixture base, have been modeled with R3D4 rigid elements.

In the frame of the numerical analyses presented here, an enhanced hourglass control has been adopted for the C3D8R finite elements. Indeed, the influence of the hourglass control parameter on the model behaviour has been monitored by comparing the artificial strain energy to the total energy. No relevant artificial strain energy (if compared to the total energy) related to deformation modes (in particular out-of-plane shear strain) has been detected during the analyses.

The contact between the impactor and the test panel has been simulated by means of a penalty-based contact algorithm. The same algorithm, enhanced with an 'all-with-self' option, has been used to avoid compenetrations between adjacent plies with fully degraded cohesive layers.

Friction between composite layers has been extensively investigated. Generally, as output from these investigations, a 0.2 friction coefficient is adopted for 0°/0° interfaces while a 0.8 friction coefficient is adopted for 0°/90° interfaces. In the present paper, as well as in some literature papers, in order to take into account also 0°/45° and 90°/45° interfaces, an averaged 0.5 friction coefficient has been adopted for all the interfaces.[49]

All the translational degrees of freedom at the edges of the local-domain have been connected to the global domain via multipoint constraints. The panel was fixed to the rigid fixture support through four rigid clamps with suppressed translational and rotational degrees of freedom while the impactor has been allowed to move only perpendicularly to

the laminate. To reduce the computation costs, a global local approach has been introduced to connect the local and global domains.[62]

In Figure 6, an exploded view of the adopted finite element model is introduced.

As already remarked, two different FEM models have been adopted in this paper. The first FEM model uses continuum shell elements both in the local and in the global domains and Hashin criteria to check for failure according to all the failure modes. The second FEM model introduces solid elements in the local domains where the implemented 3D material subroutine is applied to check for failure according to the user-defined failure criteria described in the previous section.

Experimental and numerical results

In this section, the experimental data and simulation results are correlated for the three investigated impact energy levels and for the two different numerical approaches. The impact energy values investigated and implemented in the FE code have been obtained, as already remarked, by changing the impactor

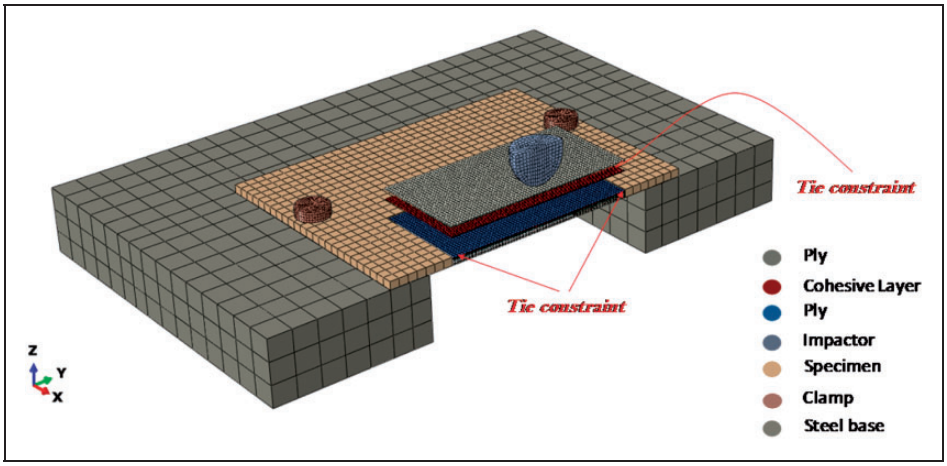

Figure 6. Exploded view of the FE model.

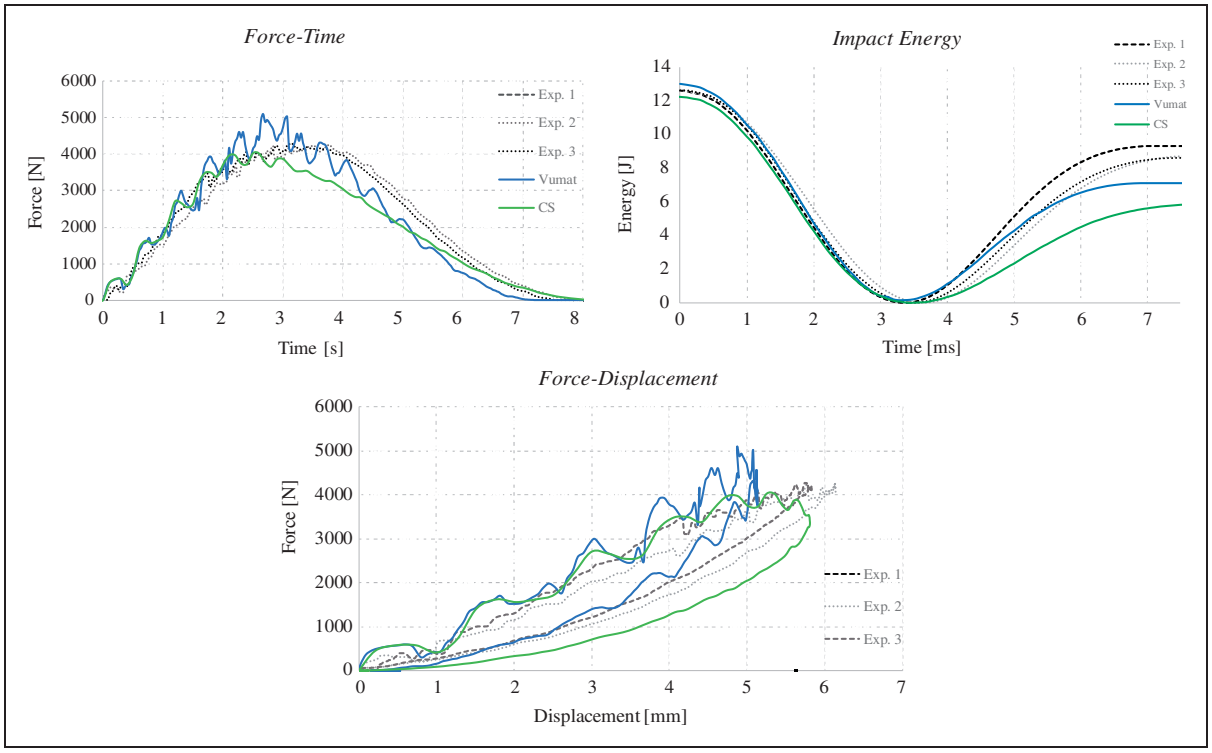

Figure 7. 13 Joule impact energy.

velocity without varying the mass. In the next figures, numerical–experimental correlations in term of impact curves (energy vs. time, impact force vs. time and impact force vs. displacements) are introduced.

For each chart, the experimental data and the numerical results obtained with the VUMAT and with the Continuum shell element formulations are reported.

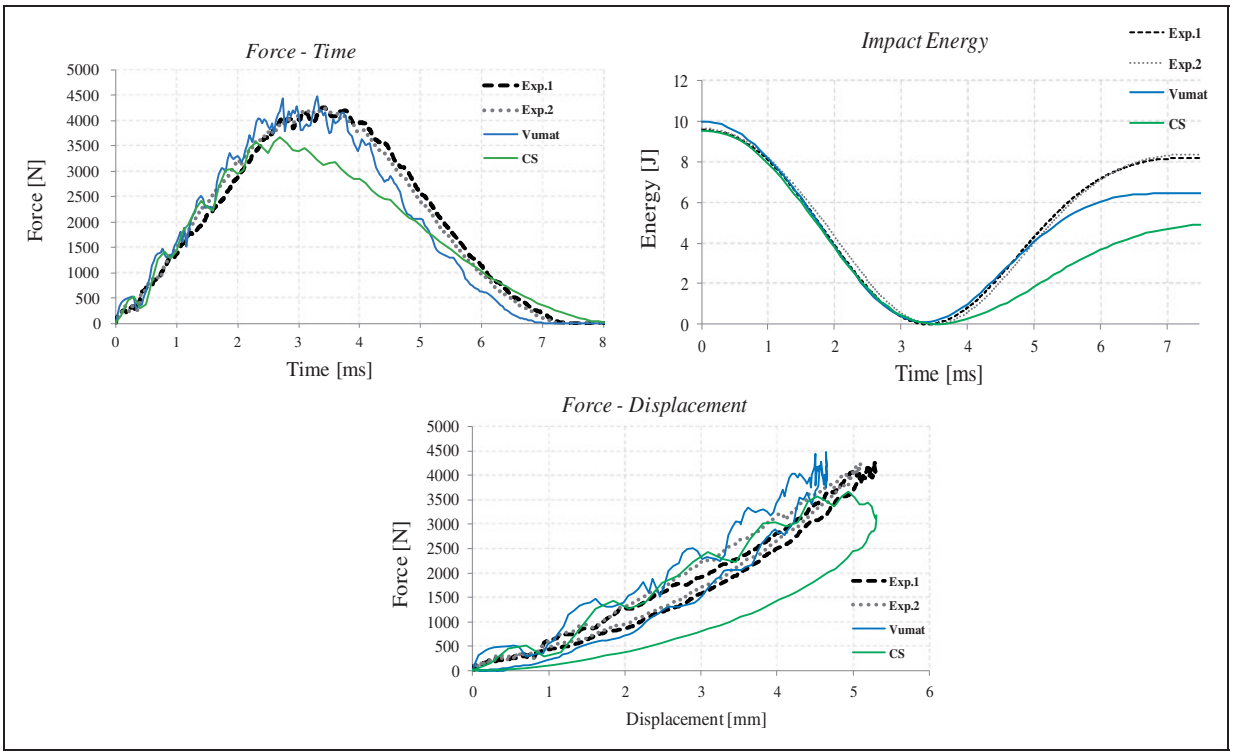

Figure 8. 10 Joule impact energy.

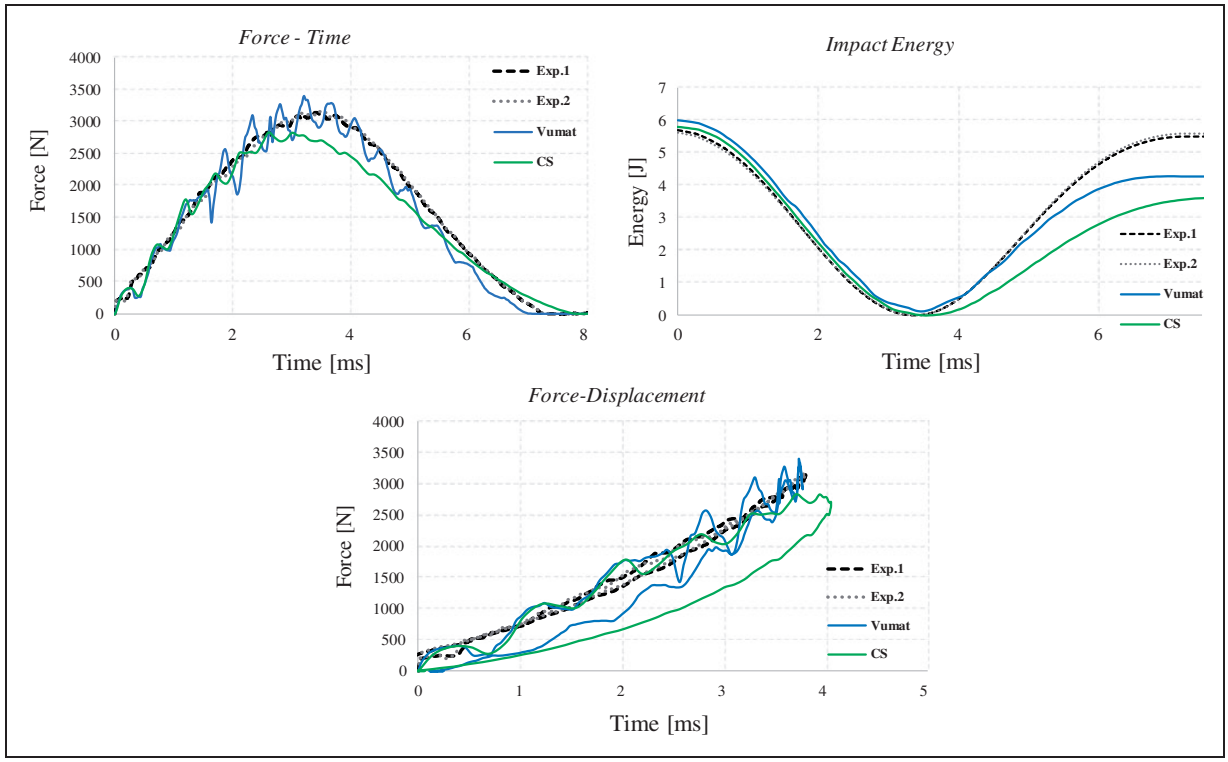

Figure 9. 6 Joule impact energy.

In particular, the force vs. time chart in Figure 7 highlights the capability of the VUMAT approach to correctly predict the force peak observed during the experimental test differently from the continuum shell elements standard approach which cannot provide a true 3D stress distribution and does not make use of non-linear shear and puck criteria. Since the area enclosed by the force vs. displacement curve is representative of the energy dissipated during the impact phenomenon, the CS model seems to overestimate the dissipated energy for the 13 J impact. On the contrary, the VUMAT model provides a more realistic prediction (15% difference with respect to experimental results) of the amount of energy dissipated by the failure mechanisms for this impact energy value. This last consideration is confirmed by the impact energy vs. time graph of Figure 7.

The accuracy of the results obtained by means of the proposed model can be also appreciated in Figure 8 where the data from the 10 J impact energy test and the results from the introduced numerical models are compared. The force vs. time plot, for this impact energy level, clearly shows that the impact behaviour predictions provided by the VUMAT model, for all the impact phenomenon duration, are again closer to experimental observations. Indeed, the continuum shell model seems to be not fully capable to correctly predict the unloading phase.

Furthermore, according to Figure 8, the proposed VUMAT numerical model, for the 10 J impact, has been found able to accurately predict the load peak recorded from the experimental test, differently from the CS model. Observing the other two plots of Figure 8 (impact energy vs. time and force vs. displacements), it can be observed that the continuum shell model significantly overestimates the dissipated energy as already seen for the 13 J impact.

For the lower energy level examined in the present work (6 J) whose numerical results and experimental data are compared in Figure 9, the same considerations, as the ones made for Figure 8, can be applied.

In addition to graphs globally describing the impact phenomenon, thermography, ultrasonic A-scan envelope and ultrasonic C-scan techniques have been used to evaluate the damage induced in the impact local area.

Figure 10 shows a comparison between all the NDT techniques outputs[51] and the results of the numerical VUMAT activity performed in this work. The results, in terms of impact-induced delaminations' envelopes length and width, are presented for the three analysed impact energy levels. An overall

Table 5. Delaminations' envelope dimensions – comparison between experimental data and numerical VUMAT results.

		Thermography	Ultrasonic A-Scan envelop	Ultrasonic C-Scan	Numerical VUMAT
6 J	Length	14 mm	20 mm	20 mm	22 mm
	Width	7 mm	15 mm	14 mm	17 mm
10 J	Length	29 mm	30 mm	33 mm	35 mm
	Width	11 mm	10 mm	17 mm	25 mm
13 J	Length	41 mm	40 mm	42 mm	39.33 mm
	Width	18 mm	22 mm	20 mm	27 mm

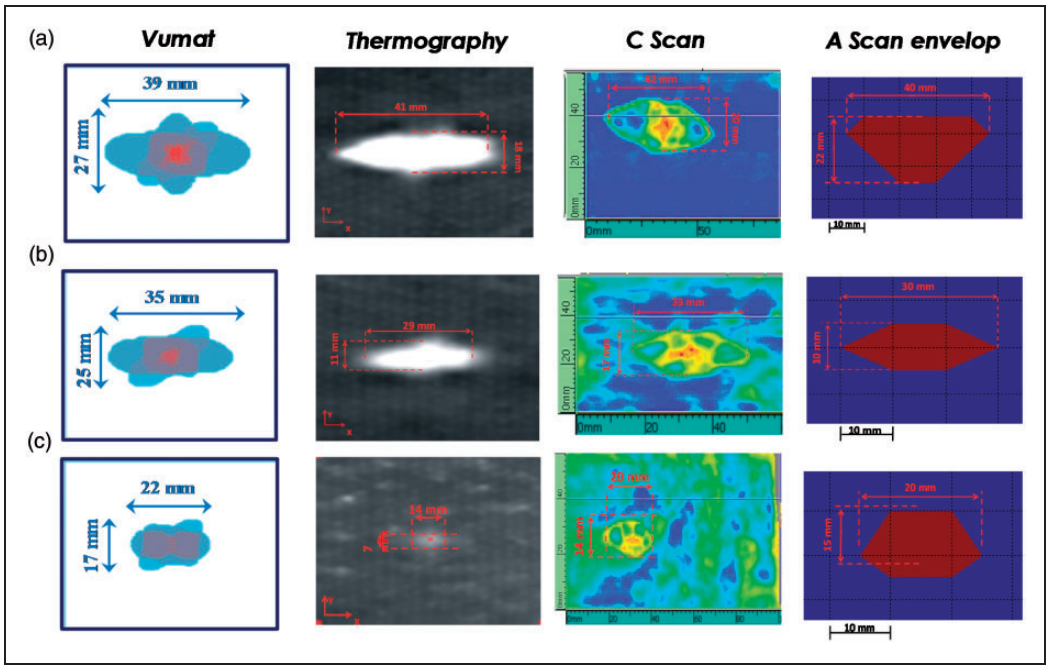

Figure 10. Comparison between NDT data[51] and numerical results in terms of delaminations' envelope: (a) 13 J impact energy; (b) 10 J impact energy and (3) 6 J impact energy.

good agreement between the VUMAT numerical and the experimental delaminations' envelope sizes can be appreciated for all the experimental non-destructive techniques and for all the impact energy levels, except for the lowest energy level, as summarised in Table 5.

Figure 11 shows the delamination envelope for the three impact energy values. The numerical results are super-imposed to the infrared thermography images. Infrared thermographic images have been preferred to ultrasonic images (able to provide an accurate picture of delaminations' depth and size), for comparison with numerical delamination envelope, due to their intrinsic feature to highlight clear delamination boundaries regardless of the delamination depth.

The images presented in Figure 11 show a good correlation in terms of shape and size, for the all the impact energy value except the lowest one, between numerical and experimental delaminations envelope. It could be highlighted that the poor correlation between numerical VUMAT and experimental delamination shape and size for the lowest impact energy level might be related to insufficient thermography instrumentations' sensitivity.

In Figure 12, the matrix traction damage plots obtained with the two proposed numerical approaches, for the three impact energy levels, are reported. Indeed the matrix traction failure mode drives the delamination formation phenomena. Hence, a good correlation in terms of shape and size of the matrix traction damaged area and delamination envelope is expected in the frame of an accurate simulation. The matrix traction damage shape and dimension obtained with the VUMAT model has been found in excellent agreement with the experimentally

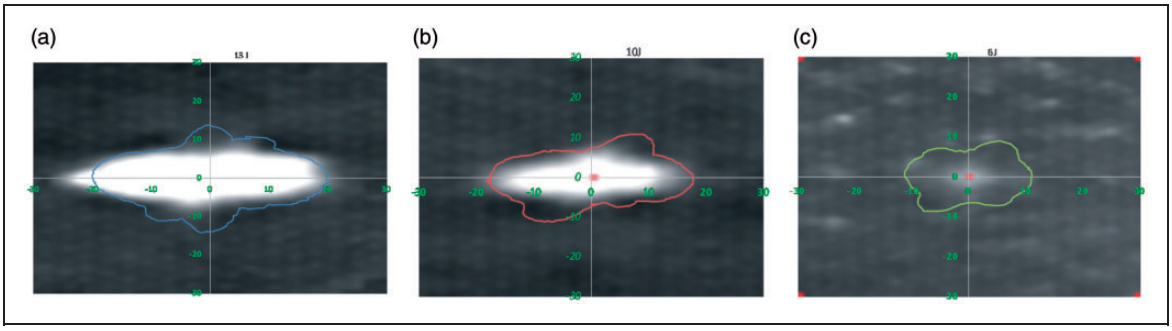

Figure 11. Thermography NDT and numerical delaminations' envelope: (a) 13 J impact energy; (b) 10 J impact energy and (c) 6 J impact energy.

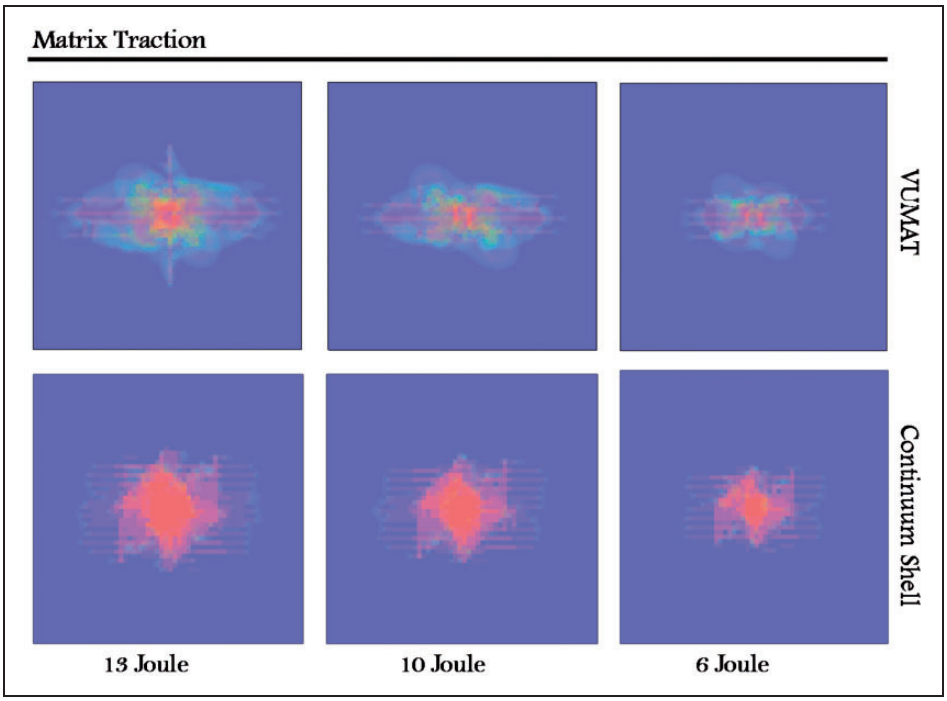

Figure 12. Matrix traction cracking overlap.

observed delamination envelope probably because the non-linear shear failure has been taken into account. On the other hand, the matrix traction damage plots obtained with the CS model show relevant discrepancies with respect to the experimentally observed impact-induced delaminations.

Conclusions

The experimental data presented in this paper in conjunction with the Non-Destructive Techniques results (thermography, A-SCAN envelope, C-SCAN) have allowed to identify the damage induced by a low velocity impact on a composite plate according to the standard prEn6038 for three different impact energy levels (13–10–6 J). The experimental numerical curves and the experimental NDT images have been correlated with numerical results obtained by means of an advanced numerical formulation involving the use of different criteria and degradation laws according to the different failure modes acting during an impact phenomenon.

Generally, the numerical results obtained by means of the standard numerical approach have been found in acceptable agreement with the experimental data. As a matter of fact, the proposed VUMAT numerical procedure provides predictions which have been found, in some cases, in excellent agreement with experimental data. However, differences between the experimental data and the VUMAT numerical model have been recorded for the lower impact energy case. These differences can be due to the complexity of the impact phenomena and to the difficulty to obtain accurate experimental measurements for the lowest impact energy levels. The use of experimental data in conjunction with numerical results has allowed to identify the progress of the induced damage and the interaction between intra-laminar and inter-laminar damage mechanisms for almost all the investigated impact energy levels.

Acknowledgements

The experimental activities presented in this paper have been performed in collaboration with The University of Naples 'Federico II' and with the 'Italian National Council of Research'. Prof Antonio Langella, Dr Vincenza Antonucci and Dr Mauro Zarrelli are acknowledged for their outstanding contribution to the research activities presented in this paper.

Declaration of Conflicting Interests

The author(s) declared no potential conflicts of interest with respect to the research, authorship, and/or publication of this article.

Funding

The author(s) received no financial support for the research, authorship, and/or publication of this article.

References

1. Tita V, de Carvalho J and Vandepitte D. Failure analysis of low velocity impact on thin composite laminates: experimental and numerical approaches. *Compos Struct* 2008; 83: 413–428.
2. Aktas M, Atas C, Icten BM, et al. An experimental investigation of the impact response of composite laminates. *Compos Struct* 2009; 87: 307–313.
3. Li C, Hu N, Yin Y, et al. Low-velocity impact-induced damage of continuous fiber-reinforced composite laminates. Part I. An FEM numerical model. *Compos Part A* 2002; 33: 1055–1062.
4. Gonzalez EV, Maimf P, Camanho PP, et al. Simulation of dropweight impact and compression after impact tests on composite laminates. *Compos Struct* 2012; 94: 3364–3378.
5. Riccio A, Raimondo A, Fragale S, et al. Delaminations buckling and growth phenomena in stiffened composite panels under compression. Part I: An experimental study. *J Compos Mater* 2014; 48: 2843–2855.
6. Riccio A, Raimondo A, Di Caprio F, et al. Delaminations buckling and growth phenomena in stiffened composite panels under compression. Part II: A numerical study. *J Compos Mater* 2014; 48: 2857–2870.
7. Choi IH. Low-velocity impact analysis of composite laminates under initial inplane load. *Compos Struct* 2008; 86: 251–257.
8. Olsson R, Donadon MV and Falzon BG. Delamination threshold load for dynamic impact on plates. *Int J Solids Struct* 2006; 43: 3124–3141.
9. Zhong Y and Joshi S. Impact behavior and damage characteristics of hygrothermally conditioned carbon epoxy composite laminates. *Mater Des* 2015; 65: 254–264.
10. Erkendirci Ö. Investigation of the quasi static penetration resistance behavior of carbon fiber reinforced laminate HDPE composites. *Compos Part B: Eng* 2016; 93: 344–351.
11. Cantwell WJ and Morton J. The impact resistance of composite materials – a review. *Composites* 1991; 22: 347–362.
12. Li Y, Zhang W, Yang Z-W, et al. Low-velocity impact damage characterization of carbon fiber reinforced polymer (CFRP) using infrared thermography. *Infrared Phys Technol* 2016; 76: 91–102.
13. Yang R and He Y. Polymer-matrix composites carbon fibre characterisation and damage inspection using selectively heating thermography (SeHT) through electromagnetic induction. *Compos Struct* 2016; 140: 590–601.
14. Bui HK, Wasselynck G, Trichet D, et al. Study on flaw detectability of NDT induction thermography technique for laminated CFRP composites. *EPJ Appl Phys* 2016; 73: article no. 10902.
15. Colombo C, Crivelli D, Gobbi G, et al. Application of thermography and acoustic emission to detect impact damage in CFRP. In: *Proceedings of the 3rd international conference of engineering against failure, ICEAF 2013*, Kos, Greece, 26–28 June 2013, pp.14–22.
16. Grimberg R, Savin A, Steigmann R, et al. Determination of CFRP's mechanical properties using ultrasound methods. In: *NDT in progress 2009 – 5th international workshop of NDT Experts, proceedings 2009*, pp.65–74.

17. Gros XE. Low energy impact detection on carbon fiber reinforced materials. *Mater Evaluat* 1995; 53: 7.
18. Abrate S. Modeling of impacts on composite structures. *Compos Struct* 2001; 51: 129–138.
19. Feraboli P and Kedward KT. A new composite structure impact performance assessment program. *Compos Sci Technol* 2006; 66: 1336–1347.
20. Lopes CS, Seresta O, Coquet Y, et al. Low-velocity impact damage on dispersed stacking sequence laminates. Part I: Experiments. *Compos Sci Technol* 2009; 69: 926–936.
21. Elder DJ, Thomson RS, Nguyen MW, et al. Review of delamination predictive methods for low speed impact of composite laminates. *Compos Struct* 2004; 66: 677–683.
22. Riccio A, Raimondo A, Borrelli R, et al. Numerical simulations of inter-laminar damage evolution in a composite wing box. *Appl Compos Mater* 2014; 21: 467–481.
23. Pietropaoli E and Riccio A. Finite element analysis of the stability (buckling and post-buckling) of composite laminated structures: well established procedures and challenges. *Appl Compos Mater* 2012; 19: 79–96.
24. Olsson R. Analytical prediction of large mass impact damage in composite laminates. *Compos Part A* 2001; 32: 1207–1215.
25. Riccio A, Di Felice G, Saputo S, et al. A numerical study on low velocity impact induced damage in stiffened composite panels. *J Computat Simulat Model* 2013; 3: 44–47.
26. Caputo F, Di Gennaro F, Lamanna G, et al. Numerical procedures for damage mechanisms analysis in CFRP composites. *Key Eng Mater* 2013; 569-570: 111–118.
27. Wisnom MR. Modelling discrete failures in composites with interface elements. *Compos A Appl Sci Manuf* 2010; 41: 795–805.
28. Riccio A, Scaramuzzino F and Perugini P. Influence of contact phenomena on embedded o in composites. *AIAA J* 2003; 41: 933–940.
29. Riccio A, Raimondo A and Scaramuzzino F. Skin stringer debonding evolution in stiffened composites under compressive load: a novel numerical approach. *KEM* 2014; 577-578: 605–608.
30. De Moura MFSF and Gonçalves JPM. Modelling the interaction between matrix cracking and delamination in carbon–epoxy laminates under low velocity impact. *Compos Sci Technol* 2004; 64: 1021–1027.
31. Lemaitre J and Chaboche J-L. *Mechanics of solid materials*. Cambridge, UK: Cambridge University Press, 1994.
32. Puck A and Schurmann H. Failure analysis of FRP laminates by means of physically based phenomenological models. *Compos Sci Technol* 1998; 58: 1045–1067.
33. Donadon MV, Iannucci L, Falzon BG, et al. A progressive failure model for composite laminates subjected to low velocity impact damage. *Comp Struct* 2008; 86: 1232–1252.
34. Falzon BG and Apruzzese P. Numerical analysis of intralaminar failure mechanisms in composite structures. Part I: FE implementation. *Compos Struct* 2011; 93: 1039–1046.
35. Pinho ST, Iannucci L and Robinson P. Physically based failure models and criteria for laminated fibre-reinforced composites with emphasis on fibre kinking. Part II: FE implementation. *Compos Part A: Appl Sci Manuf* 2006; 37: 766–777.
36. Tay TE. Characterization and analysis of delamination fracture in composites: an overview of developments from 1990 to 2001. *Appl Mech Rev* 2003; 56: 1–32.
37. Camanho PP, Davila CG and De Moura MF. Numerical simulation of mixed-mode progressive delamination in composite materials. *J Compos Mater* 2003; 37: 1415–1438.
38. Riccio A, Raimondo A and Scaramuzzino F. A study on skin delaminations growth in stiffened composite panels by a novel numerical approach. *Appl Compos Mater* 2013; 20: 465–488.
39. Aymerich F, Dore F and Priolo P. Simulation of multiple delaminations in impacted cross-ply laminates using a finite element model based on cohesive interface elements. *Compos Sci Technol* 2009; 69: 1699–1709.
40. Amaro AM, Santos JB and Cirne JS. Delamination depth in composites laminates with interface elements and ultrasound analysis. *Strain* 2011; 47: 138–145.
41. Bouvet C, Rivallant S and Barrau JJ. Low velocity impact modeling in composite laminates capturing permanent indentation. *Compos Sci Technol* 2012; 72: 1977–1988.
42. Aoki Y, Suemasu H and Ishikawa T. Damage propagation in CFRP laminates subjected to low velocity impact and static indentation. *Adv Compos Mater* 2007; 16: 45–61.
43. Aymerich F, Dore F and Priolo P. Prediction of impact-induced delamination in cross-ply composite laminates using cohesive interface elements. *Compos Sci Technol* 2008; 68: 2383–2390.
44. Bouvet C, Castanié B, Bizeul M, et al. Low velocity impact modelling in laminate composite panels with discrete interface elements. *Int J Solids Struct* 2009; 46: 2809–2821.
45. Bouvet C, Hongkarnjanakul N, Rivallant S, et al. Discrete impact modeling of inter- and intra-laminar failure in composites. In: Abrate S, Castanié B and Rajapakse YDS (eds) *Dynamic failure of composite and sandwich structures*. Dordrecht: Springer, 2013, pp.339–392.
46. de Borst, Remmers JJ and Needleman A. Mesh-independent discrete numerical representations of cohesive-zone models. *Eng Fract Mech* 2006; 73: 160–177.
47. Iannucci L. Progressive failure modelling of woven carbon composite under impact. *Int J Impact Eng* 2006; 32: 1013–1043.
48. Maimí P, Camanho PP, Mayugo JA, et al. A continuum damage model for composite laminates: Part I – constitutive model. *Mech Mater* 2007; 39: 897–908.
49. Shi Y, Swait T and Soutis C. Modelling damage evolution in composite laminates subjected to low velocity impact. *Compos Struct* 2012; 94: 2902–2913.
50. Riccio A, Ricchiuto R, Saputo S, et al. Impact behaviour of omega stiffened composite panels. *Progr Aerosp Sci* 2016; 81: 41–48.
51. Riccio A, Caputo F, Di Felice G, et al. A Joint Numerical-Experimental Study on Impact Induced Intra-laminar and Inter-laminar Damage in Laminated Composites. Applied Composite Materials. *Appl Compos Mater* 2015; 23: 219–237.

52. Hashin Z. Failure criteria for unidirectional fiber composites. *J Appl Mech* 1980; 47: 329–334.
53. Fuossa E, Straznicky PV and Poonb C. Effects of stacking sequence on the impact resistance in composite laminates – Part 1: parametric study. *Compos Struct* 1998; 41: 66–67.
54. Fanteria D, Longo G and Panettieri E. A non-linear shear damage model to reproduce permanent indentation caused by impacts in composite laminates. *Compos Struct* 2014; 111: 111–121.
55. Arslan S, Sadeghi MZ, Dafnis A, et al. Investigation in the mechanical behavior of lowvelocity impacted cfrp plates under different boundary conditions. In: Papadrakakis M, Papadopoulos V, Stefanou G, (eds) *VII European Congress on Computational Methods in Applied Sciences and Engineering, ECCOMAS Congress 2016*, Crete Island, Greece, 5–10 June 2016.
56. Davila CG, Camanho PP and Turon A. Cohesive elements for shells. NASA Report, NASA/TP-2007-2148869, 2007, pp.1–27.
57. Bazant ZP and Oh BH. Crack band theory for fracture of concrete. *Mat Struct* 1983; 16: 155–177.
58. Feng D and Aymerich F. Finite element modelling of damage induced by low-velocity impact on composite laminates. *Compos Struct* 2014; 108: 161–171.
59. ABAQUS Analysis User's Manual 6.11, 2011.
60. Turon A, Dávila CG, Camanho PP, et al. An engineering solution for solving mesh size effects in the simulation of delamination with cohesive zone models. *Eng Fract Mech* 2007; 74: 1665–1682.
61. Panettieri E, Fanteria D and Danzi F. A sensitivity study on cohesive elements parameters: towards their effective use to predict delaminations in low-velocity impacts on composites. *Compos Struct* 2016; 137: 130–139.
62. Sellitto A, Borrelli R, Caputo F, et al. Methodological approaches for kinematic coupling of non-matching finite element meshes. *Proc Eng* 2011; 10: 421–426.